ADVANCED PHOTONICS RESEARCH Open Access
www.adpr-journal.com

Tunable Dual-Band White Light Emission from Gua_3CuCl_4 and $Gua_7Cu_3X_{10}{\cdot}3DMF$ (X = Br, I)

*Isaiah W. Gilley, Tielyr D. Creason, Timothy M. McWhorter, and Bayram Saparov**

All-inorganic copper(I) halides have recently emerged as attractive alternatives to lead-based halide perovskites and rare-earth-doped inorganics for light emission applications. Most of the newly discovered all-inorganic Cu(I) halides demonstrate high-efficiency blue emission albeit with unusually poor tunability of photoluminescence (PL) properties. This work reports the facile preparation of three new copper(I) halides based on the guanidinium cation: $(CN_3H_6)_3CuCl_4$, $(CN_3H_6)_7Cu_3Br_{10}{\cdot}3(C_3H_7NO)$, and $(CN_3H_6)_7Cu_3I_{10}{\cdot}3(C_3H_7NO)$. A comprehensive characterization of PL is presented for these novel materials, which have highly tunable, dual blue–yellow emission responsive to both excitation wavelength and vacuum annealing. These have remarkable photoluminescence quantum yield (PLQY) values of up to 34.6% and color-rendering indices (CRI) up to 97% for tunable, single-phase white light emission with correlated color temperatures (CCT) ranging from 4851 to 18 921 K, demonstrating the excellent potential of Cu(I) halides for light emission applications.

1. Introduction

The pursuit of highly efficient luminescent materials for solid-state lighting and radiation detection has recently been expanded to include all-inorganic and hybrid organic–inorganic metal halides.[1] Ternary lead halides, such as cesium and methylammonium lead halide perovskites, have been lauded for their high efficiencies, but the mass production and distribution of lead-containing compounds is a significant environmental concern, and lead-halide perovskites often have air and moisture stability problems.[1d,1g,2] Ternary copper(I) halides have thus emerged as alternative Pb-free materials, with the blue-emitting $A_3Cu_2X_5$ and A_2CuX_3 (A = K, Rb, Cs; X = Cl, Br, I) families exhibiting record high photoluminescence quantum yield (PLQY) values of up to 100% at room temperature.[1b,1d,2g,3] However, most of these high-efficiency all-inorganic copper(I) emitters show poor tunability of their photoluminescence (PL) properties with blue emission patterns being characteristic of the family. Furthermore, substitutions of the A and X sites in these all-inorganic copper(I) halides yield minimal change to their PL spectra, an unusual trait for metal halides.[1d,2g] This poor PL tunability is generally attributed to a domination of the conduction band minimum (CBM) and valence band maximum (VBM) energy states by copper(I) orbitals in their electronic band structures.[1d,2g] Therefore, substitution of copper(I) with silver(I) was recently explored in a series of A_2AgX_3 compounds to gain control over the PL properties in these families.[4]

Yet another distinct approach to solving the problem of poor PL tunability in ternary copper(I) halides is to focus on hybrid organic–inorganic compositions, replacing the alkali-metal A^+ cation with an organic cation.[5] The virtually unlimited variety of organic cations of differing sizes, shapes, and electronic properties provides a wealth of selections, allowing specific targeting of organic cations that can directly or indirectly impact the light emission in copper(I) halides. To demonstrate the viability of this approach, here we report the synthesis and characterization of new ternary hybrid copper(I) halides Gua_3CuCl_4 and $Gua_7Cu_3X_{10}{\cdot}3DMF$ (X = Br, I) (Gua = guanidinium, $[CN_3H_6]^+$). In this work, the guanidinium cation was selected because its resonance-stabilized charge is distributed uniformly across its three nitrogen atoms, resulting in a "disc" of positive charge with a diameter of approximately 3.6 Å. The weak charge distribution of guanidinium allows it to serve as an element in exploring the effects of large, weakly charged A organic cations on the photophysical properties of ternary copper(I) halides. Previous attempts to integrate guanidinium in luminescent materials have resulted in dramatic changes in PL properties over corresponding all-inorganic systems, including multiple broad blue- and green-emitting $Gua_3Cu_2I_5$ phases with increased PL tunability and PLQY up to 93%, which suggests that the use of organic cations in hybrid Cu(I) halides is an effective way to bring tunability of PL properties.[6]

The new compounds reported in this work, Gua_3CuCl_4 and $Gua_7Cu_3X_{10}{\cdot}3DMF$, show dramatically different light emission properties compared to all-inorganic copper(I) halides; $Gua_7Cu_3Br_{10}{\cdot}3DMF$ and $Gua_7Cu_3I_{10}{\cdot}3DMF$ exhibit dual-band PL emission spectra including a broad, low energy emission peak in addition to the narrow blue emission characteristic of other luminescent copper(I) halides.[1d,2g] The resulting broadband

I. W. Gilley, T. D. Creason, T. M. McWhorter, B. Saparov
Department of Chemistry and Biochemistry
University of Oklahoma
101 Stephenson Parkway, Norman, OK 73019, USA
E-mail: saparov@ou.edu

The ORCID identification number(s) for the author(s) of this article can be found under https://doi.org/10.1002/adpr.202200172.

© 2022 The Authors. Advanced Photonics Research published by Wiley-VCH GmbH. This is an open access article under the terms of the Creative Commons Attribution License, which permits use, distribution and reproduction in any medium, provided the original work is properly cited.

DOI: 10.1002/adpr.202200172

Downloaded from SHAREOK. Persistent Handle URL: https://hdl.handle.net/11244/336539

26999293, 0, Downloaded from https://onlinelibrary.wiley.com/doi/10.1002/adpr.202200172, Wiley Online Library on [16/10/2022]. See the Terms and Conditions (https://onlinelibrary.wiley.com/terms-and-conditions) on Wiley Online Library for rules of use; OA articles are governed by the applicable Creative Commons License

PL is highly tunable, with $Gua_7Cu_3I_{10}$·3DMF having a PLQY value up to 34.6% and color-rendering index (CRI) as high as 97% for near-sunlight 4851 K correlated color temperature (CCT) emission. The dual emissions of $Gua_7Cu_3Br_{10}$·3DMF and $Gua_7Cu_3I_{10}$·3DMF are attributed to a multiexcitonic emission with contribution from defect-bound excitons (DBEs) and self-trapped excitons (STEs), explaining the PL tunability uncommon in other ternary copper(I) halides. The DBE emission observed in $Gua_7Cu_3Br_{10}$·3DMF and $Gua_7Cu_3I_{10}$·3DMF is attributed to halogen vacancies, an assignment that is supported by experiments performed on $Gua_7Cu_3I_{10}$·3DMF. Simultaneous STE and DBE emission has been previously observed in the related A_2AgX_3 family (A = Rb, Cs; X = Cl, Br, I).[4a] Additionally, we report anti-Stokes photoluminescence (ASPL) characterization of Gua_3CuCl_4 and $Gua_7Cu_3X_{10}$·3DMF, which show anti-Stokes shifts as wide as 0.6462 eV. We also observe a strong energetic correlation between anti-Stokes photoluminescence excitation (ASPLE) and the DBE emission mentioned above, suggesting a connection between the anti-Stokes excitation and halide vacancies within these materials. Overall, the experimental work presented shows that hybrid copper(I) halides present an exciting new class of highly luminescent tunable broadband emitters.

2. Results and Discussion

Gua_3CuCl_4 crystallizes in the orthorhombic $Pna2_1$ space group with a structure consisting of 0D $[CuCl_4]^{3-}$ tetrahedra arranged in pseudochains spanning the [110] direction with guanidinium ions filling the space around and between the chains. A projection of the crystal structure for Gua_3CuCl_4 down the *b*-axis is shown in **Figure 1**. Neighboring tetrahedra within each chain are separated by 4.365 Å. The $[CuCl_4]^{3-}$ tetrahedra are distorted, with Cu—Cl bond distances ranging from 2.3142(13) to 2.3708(13) Å and Cl—Cu—Cl bond angles ranging from 102.88(5) to 119.62(5)°. This structure represents a drop in dimensionality from the high-efficiency blue emitting A_2CuX_3 (A = K, Rb; X = Cl, Br, I) family, which exhibit 1D crystal structures containing copper(I) halide corner-sharing tetrahedral chains.[1d,2g] The distortion seen in the copper(I) chloride tetrahedra of Gua_3CuCl_4 is similar to that seen in A_2CuCl_3, while the Cu—Cl bonds are slightly shorter at a minimum of 2.3142(13) Å in Gua_3CuCl_4, 2.3319(4) Å in K_2CuCl_3, and 2.3363(6) Å in Rb_2CuCl_3.[1d,2g] A similar comparison is made with the $CsCu_2X_3$ (X = Cl, Br, I) family, which crystallizes in the orthorhombic *Cmcm* space group with edge sharing tetrahedral $[Cu_2X_3]^-$ chains separated by rows of Cs^+ cations.[3a] The variance in Cu—Cl bond lengths is less in $CsCu_2Cl_3$ than in Gua_3CuCl_4 while the minimum Cu—Cl bond length is slightly shorter (2.272(8) Å in $CsCu_2Cl_3$).[3a] The tetrahedra show a nearly identical level of distortion between $CsCu_2Cl_3$ and Gua_3CuCl_4, with Cl—Cu—Cl bond angles in $CsCu_2Cl_3$ ranging from 102.44(9) to 119.30(9)°.[3a]

In contrast, the heavier copper(I) bromide derivative $Gua_7Cu_3Br_{10}$·3DMF has a distinct, more complex structure type in the trigonal *P*31*c* space group. The structure of $Gua_7Cu_3Br_{10}$·3DMF consists of four distinct pseudochains arranged in a honeycomb-like hexagonal pattern extending down the *c*-axis (**Figure 2**). The four chains are labeled as: 1) alternating tetrahedral $[CuX_7]^{5-}$ dimers and guanidinium molecules with a repetition period of 14.271 Å, 2) parallel, trigonal planar $[CuX_3]^{2-}$ units with a spacing of 7.136 Å, 3) guanidinium molecules with alternating orientation and a spacing of 7.136 Å, and 4) parallel, alternating DMF and guanidinium molecules with a spacing of 3.568 Å. The arrangement of these chains is shown in Figure S1, Supporting Information, where chains 1, 2, and 3 comprise the vertices of the honeycomb pattern, while chain 4 fills the hexagonal gaps. In $Gua_7Cu_3Br_{10}$·3DMF, the trigonal planar $[CuBr_3]^{2-}$ units have regular Cu—Br bond lengths of 2.3758(8) Å and Br—Cu—Br bond angles of 120°, while the tetrahedral $[Cu_2Br_7]^{5-}$ dimers are slightly distorted with Cu—Br bond

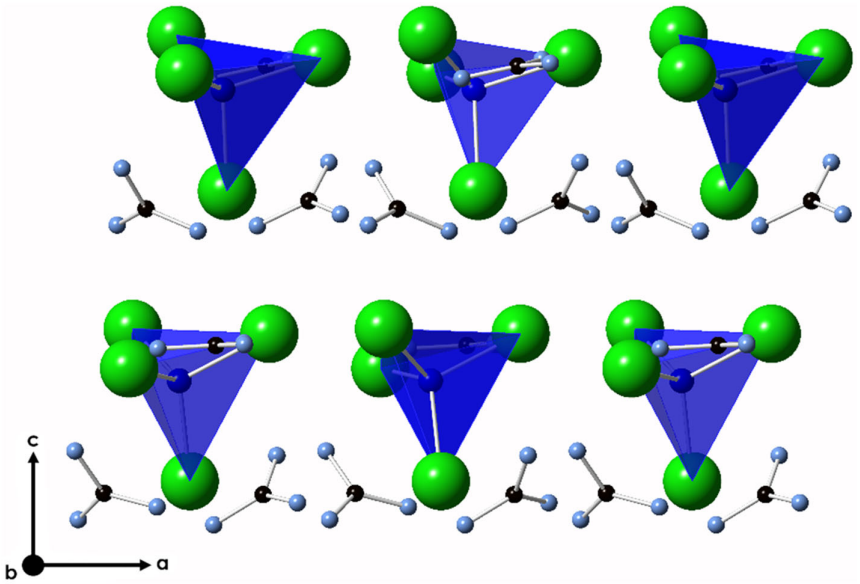

Figure 1. Polyhedral model of the 0D structure of Gua_3CuCl_4 projected down the *b*-axis.

© 2022 The Authors. Advanced Photonics Research published by Wiley-VCH GmbH

26999293, 0, Downloaded from https://onlinelibrary.wiley.com/doi/10.1002/adpr.202200172, Wiley Online Library on [16/10/2022]. See the Terms and Conditions (https://onlinelibrary.wiley.com/terms-and-conditions) on Wiley Online Library for rules of use; OA articles are governed by the applicable Creative Commons License

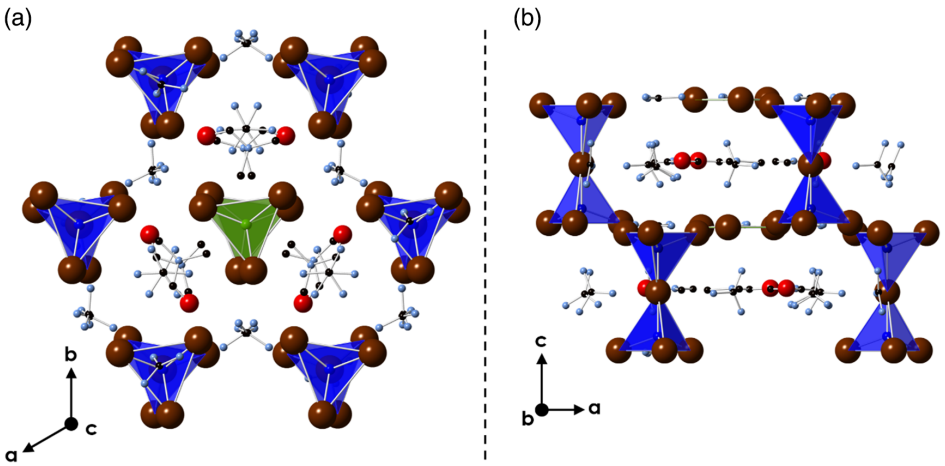

Figure 2. Polyhedral model of the 0D structure of $Gua_7Cu_3Br_{10}$·3DMF projected down the a) *c*-axis and b) *b*-axis. Tetrahedral dimer $[Cu_2Br_7]^{5-}$ units are colored in blue, trigonal planar $[CuBr_3]^{2-}$ units are colored in green, and carbon, nitrogen, oxygen, and bromine are colored black, light blue, red, and brown, respectively. Hydrogens have been omitted from the model to improve visual clarity.

lengths ranging from 2.450(2) to 2.4889(9) Å and Br—Cu—Br bond angles ranging from 108.58(4)° to 110.35(4)°. However, the tetrahedral distortion seen in these dimers is much less than in the isolated tetrahedra of Gua_3CuCl_4.

Interestingly, copper(I) forms two distinct polyhedral units within $Gua_7Cu_3Br_{10}$·3DMF: a corner-sharing tetrahedral $[Cu_2Br_7]^{5-}$ dimer and a trigonal planar $[CuBr_3]^{2-}$ unit. While similar structures were reported in the $Cs_3Cu_2X_5$ (X = Cl, Br, I) family,[7] where a $[Cu_2X_5]^{3-}$ unit is composed of a tetrahedron sharing an edge with a trigonal planar subunit, the presence of two different, isolated metal halide polyhedral units in a crystal structure containing only one B metal cation is rare.[1d,1k,2g,3a,4a,5c,6,8] Since in all-inorganic copper(I) halides, Cu(I) orbitals are dominant contributors to the states around the bandgap,[1d,2g,3a] the presence of two very different copper(I) coordination sites has interesting implications for luminescence in $Gua_7Cu_3Br_{10}$·3DMF, where the potential for either or both copper(I) sites to luminesce is present. Also notable is the presence of DMF solvent molecules within the crystal structure of $Gua_7Cu_3Br_{10}$·3DMF, where the DMF molecules occupy regular crystallographic sites, alternating with guanidinium molecules in the fourth chain of Figure S1, Supporting Information, which is contrary to the usual observation that solvent molecules increase structural disorder.[9]

The crystallization of $Gua_7Cu_3Br_{10}$·3DMF in a trigonal space group represents a structural departure from all other reported luminescent ternary copper halides, which crystallize in orthorhombic and monoclinic space groups.[1d,1i,2g,3a,5c,6a–c] Nevertheless, $Gua_7Cu_3Br_{10}$·3DMF shares certain structural similarities with the previously reported $MA_4Cu_2Br_6$, which also has 0D tetrahedral dimers and crystallizes in the triclinic $P\bar{1}$ space group.[5c] Unlike $Gua_7Cu_3Br_{10}$·3DMF, however, the tetrahedral dimers in $MA_4Cu_2Br_6$ are edge-sharing $[Cu_2Br_6]^{4-}$ rather than corner-sharing $[Cu_2Br_7]^{5-}$. The Cu—Br bond lengths in $Gua_7Cu_3Br_{10}$·3DMF and $MA_4Cu_2Br_6$ are comparable, with slightly longer Cu—Br bonds of 2.4363(3) Å observed in $MA_4Cu_2Br_6$, and the tetrahedral bond angles are slightly less distorted in $MA_4Cu_2Br_6$, where they range from 103.602(12) to 113.211(13)°. One major structural difference between these two materials, however, is the arrangement of organic cations, with $MA_4Cu_2Br_6$ having methylammonium cations separating all adjacent pairs of tetrahedral $[Cu_2Br_6]^{4-}$ dimers while $Gua_7Cu_3Br_{10}$·3DMF has guanidinium cations arranged into pseudochains. Overall, while $Gua_7Cu_3Br_{10}$·3DMF is unique among other luminescent ternary copper(I) halides, it is most structurally similar to $MA_4Cu_2Br_6$, which showed broad luminescence centered at 524 nm and PLQY up to 93%.[5c]

Slow cooling in DMF produces ostensibly high-quality single block crystals of $Gua_7Cu_3I_{10}$·3DMF, photographs of which are shown in Figure S2, Supporting Information. However, elucidation of a crystal structure from single-crystal X-ray diffraction (SCXRD) data taken with these crystals has proved exceedingly difficult, with only a partial structural solution being achieved. This difficulty is largely attributed to the extreme air-sensitivity of $Gua_7Cu_3I_{10}$·3DMF. Nevertheless, the inorganic lattice of $Gua_7Cu_3I_{10}$·3DMF found in the partial structural solution proved identical to that of $Gua_7Cu_3Br_{10}$·3DMF, which can be seen in Figure S3, Supporting Information. Finally, the measured powder X-ray diffraction (PXRD) pattern of $Gua_7Cu_3I_{10}$·3DMF, shown in Figure S4, Supporting Information, appears as a rigid shift of the PXRD pattern of $Gua_7Cu_3Br_{10}$·3DMF. This evidence leads us to tentatively conclude that the crystal structure of $Gua_7Cu_3I_{10}$·3DMF is very similar, if not isostructural, to that of $Gua_7Cu_3Br_{10}$·3DMF.

Slow cooling in hydrochloric acid produces single block crystals of Gua_3CuCl_4 up to 0.5 cm long while slow cooling in DMF produces single block crystals of $Gua_7Cu_3X_{10}$·3DMF up to 1 cm long. Notably, attempted slow cooling of Gua_3CuCl_4 in DMF produces a low-quality, impure product, and slow cooling of GuaX and CuX in the corresponding hydrohalic acid produces previously reported $Gua_4Cu_4Br_8$ and $Gua_3Cu_2I_5$ with noticeable impurities.[6c] Bulk purity of these samples was confirmed by thoroughly grinding single crystals for room-temperature PXRD measurements. Based on these

© 2022 The Authors. Advanced Photonics Research published by Wiley-VCH GmbH

26999293, 0, Downloaded from https://onlinelibrary.wiley.com/doi/10.1002/adpr.202200172, Wiley Online Library on [16/10/2022]. See the Terms and Conditions (https://onlinelibrary.wiley.com/terms-and-conditions) on Wiley Online Library for rules of use; OA articles are governed by the applicable Creative Commons License

measurements, synthesis by slow cooling in DMF produces high purity samples with only minor impurities related to degradation in air when measuring PXRD. Room-temperature PXRD measurements were also used to monitor the structural stability, for which there are two major concerns: the tendency of copper(I) to oxidize to copper(II)[2g] and the extreme hygroscopicity of guanidinium halides.[10] To evaluate air stability of $Gua_7Cu_3X_{10}{\cdot}3DMF$, powdered samples were exposed to ambient laboratory conditions (20 °C with a relative humidity of 30%) for a period of 24 h during which regular room-temperature PXRD measurements were taken. These measurements showed that 24 h exposure to air resulted in near total degradation of the samples, with significant structural changes being observed within the first hour of exposure. PXRD patterns for $Gua_7Cu_3X_{10}{\cdot}3DMF$ are shown in Figure S4 and S5, Supporting Information, and an air stability PXRD plot for $Gua_7Cu_3Br_{10}{\cdot}3DMF$ is shown in Figure S6, Supporting Information.

Thermal stability of $Gua_7Cu_3Br_{10}{\cdot}3DMF$ and $Gua_7Cu_3I_{10}{\cdot}3DMF$ was determined by simultaneous thermogravimetric analysis (TGA) and differential scanning calorimetry (DSC) shown in Figure S7, Supporting Information. Results from these measurements showed two distinct thermal events for each sample. For $Gua_7Cu_3Br_{10}{\cdot}3DMF$, the first thermal event is seen at 85.85 °C. This event corresponds to the experimentally determined melting point for $Gua_7Cu_3Br_{10}{\cdot}3DMF$ of approximately 85 °C. The weight loss accompanying this transition is 12.5%, which is attributed to partial evaporation of the liquid sample. A second thermal event is observed for $(CN_3H)_6Cu_2Br_8$ at 334.04 °C, which matches the experimentally determined boiling point for $Gua_7Cu_3Br_{10}{\cdot}3DMF$ of approximately 320 °C. This DSC transition is mirrored in the TGA measurement, which shows a gradual weight loss corresponding to vaporization of remaining GuaBr and DMF. For $Gua_7Cu_3I_{10}{\cdot}3DMF$, two similar thermal events are observed at 68.33 and 332.92 °C. The first has a corresponding weight loss of 11.9%, which is again attributed to partial evaporation of liquid $Gua_7Cu_3I_{10}{\cdot}3DMF$, which has an experimentally determined melting point around 67 °C. The second thermal event at 332.92 °C corresponds to the weight loss of remaining GuaI and DMF as the compound begins to boil at 315 °C.

Evaluations of optical properties for Gua_3CuCl_4 and $Gua_7Cu_3X_{10}{\cdot}3DMF$ were made using room-temperature photoluminescence excitation (PLE) and PL emission measurements **(Figure 3)**. A plot of the CIE 1931 color coordinates for each emission spectrum is shown in **Figure 4**. Notably, the emission patterns for $Gua_7Cu_3Br_{10}{\cdot}3DMF$ and $Gua_7Cu_3I_{10}{\cdot}3DMF$ vary over time, with fresh samples showing primarily narrow, blue emission characteristic of previously reported ternary copper(I) halides[1d,1k,2g,3a,5a] while the same samples develop secondary green emission after 1 week in a nitrogen-filled glove box. Moreover, the speed and magnitude of the development of this secondary emission is affected by halide substitution, with Gua_3CuCl_4 showing no change in recorded in PL, $Gua_7Cu_3Br_{10}{\cdot}3DMF$ developing a distinct shoulder in its PL pattern, and the blue emission of fresh $Gua_7Cu_3I_{10}{\cdot}3DMF$ being completely replaced by a single, green emission, each in the span of 1 week. These changing PL properties are uncharacteristic of other ternary copper(I) halides, which tend to have PL spectra that vary little with time or halide substitution, the latter of which being explained by the fact that the conduction band minimum (CBM) and valence band maximum (VBM) energy state densities for these compounds are generally dominated by copper(I) orbitals in their electronic band structures.[1d,2g,3a,11]

The PL spectra seen in Figure 3 show Gua_3CuCl_4 exhibits narrow, blue emission with a maximum at 445 nm and a full width at half maximum (FWHM) of 69 nm, and the corresponding excitation maximum is at 279 nm. This transition is also seen in the pseudoabsorbance spectrum of powdered Gua_3CuCl_4 in Figure S8a, Supporting Information, which has a transition approximated at 4.07 eV, measured by the intersection of the two fitted lines as described in Makuła et al.[12] The secondary minor transition fitted to 2.51 eV is attributed to contamination by GuaCl, but this minor transition is not reflected in the PL spectrum of Gua_3CuCl_4, which is expected as GuaCl shows no significant emission in the 250–750 nm range under the same measurement conditions. Fresh $Gua_7Cu_3Br_{10}{\cdot}3DMF$ exhibits a similar yet slightly blueshifted PL peak with an emission maximum at 426 nm, a corresponding FWHM of 63 nm, and an excitation maximum at 303 nm. This is mirrored in the pseudo-absorbance spectrum shown in Figure S8b, Supporting Information, which has a bandgap approximation of 4.02 eV. However, after 1 week in a nitrogen-filled glove box, $Gua_7Cu_3Br_{10}{\cdot}3DMF$ develops a secondary emission shoulder with a maximum at 517 nm while the PLE maximum shifts slightly to 309 nm.

This two-peak emission is indicative of a multiexciton emission; in this case, a combination of high energy STE and low energy DBE emissions, which we attribute to bromide vacancies (V_{Br}^{+}). The assignment of this secondary emission to halogen vacancies is supported by the fact that the formation of the defect PL peak is accelerated by exposure to vacuum. The same PL transformation seen in $Gua_7Cu_3Br_{10}{\cdot}3DMF$ after 1 week in a nitrogen-filled glovebox (Figure 3b,c) was observed when a fresh sample was exposed to vacuum for only 2 days. This observation is consistent with previously reported literature, which suggests that exposure to vacuum during and after crystal formation increases the prevalence of halide vacancies.[4a,13] Furthermore, to test whether the observed change in PL over time was the result of a phase transition, we compared PXRD patterns of a sample of $Gua_7Cu_3Br_{10}{\cdot}3DMF$ before and after 4 days in vacuum (Figure S9, Supporting Information). Here, we found that while the intensity of the PXRD pattern was reduced after vacuum treatment, no new peaks appeared in the pattern, indicating that vacuum exposure reduced the crystallinity of the sample but did not induce a structural phase transition. This observation supports the attribution of this PL change over time to the formation of defects within the crystals, a large concentration of which would result in reduced crystallinity. The attribution of similar dual emission to a combination of STEs and DBEs was previously reported for $(NH_4)_2AgBr_3$ and Rb_2AgBr_3 but has not yet been reported in copper halides.[4]

In comparison, fresh $Gua_7Cu_3I_{10}{\cdot}3DMF$ shows dual emission even before vacuum exposure, with a PL maximum at 434 nm and a shoulder centered at approximately 530 nm, resulting in a broader FWHM of 94 nm. The PLE is centered at 314 nm and consistent with the pseudoabsorbance plot for $Gua_7Cu_3I_{10}{\cdot}3DMF$ (Figure S8c, Supporting Information), which

© 2022 The Authors. Advanced Photonics Research published by Wiley-VCH GmbH

26999293, 0, Downloaded from https://onlinelibrary.wiley.com/doi/10.1002/adpr.202200172, Wiley Online Library on [16/10/2022]. See the Terms and Conditions (https://onlinelibrary.wiley.com/terms-and-conditions) on Wiley Online Library for rules of use; OA articles are governed by the applicable Creative Commons License

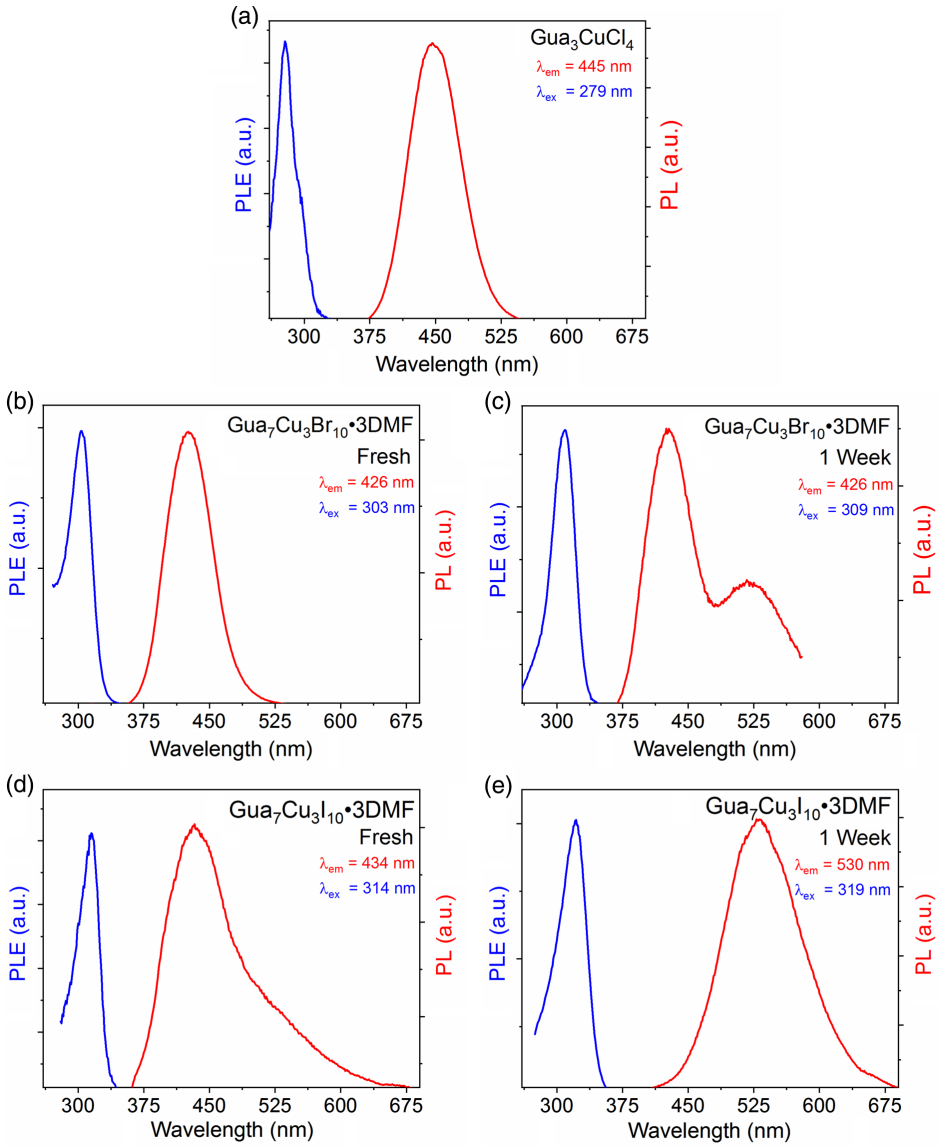

Figure 3. Room-temperature PLE (blue lines) and PL emission (red lines) spectra of single crystals of a) Gua_3CuCl_4, b) fresh $Gua_7Cu_3Br_{10}$·3DMF, c) $Gua_7Cu_3Br_{10}$·3DMF after 1 week in a nitrogen-filled glove box, d) fresh $Gua_7Cu_3I_{10}$·3DMF, and e) $Gua_7Cu_3I_{10}$·3DMF after 1 week in glove box, with emission maxima shown in red and excitation maxima shown in blue.

has a major transition approximated at 3.86 eV and a minor transition at 2.93 eV, attributed to the major and minor PL centers, respectively. Like $Gua_7Cu_3Br_{10}$·3DMF, we attribute the high energy and low energy emission centers of $Gua_7Cu_3I_{10}$·3DMF to STE and DBE emission due to iodide vacancies (V_I^+), respectively. Also, like $Gua_7Cu_3Br_{10}$·3DMF, the PL spectrum of $Gua_7Cu_3I_{10}$·3DMF changes significantly over 1 week in nitrogen atmosphere. However, while the PL spectrum of $Gua_7Cu_3Br_{10}$·3DMF transitions from a single high energy peak to dual emission, the PL of $Gua_7Cu_3I_{10}$·3DMF reduces from dual emission to a single, low energy peak centered at 530 nm with a FWHM of 103 nm. This indicates that the secondary, low energy emission shoulder seen in the PL of fresh $Gua_7Cu_3I_{10}$·3DMF eventually dominates the emission. This observation is consistent with the fact that the DBE state is at an apparently lower energy level than the STE state; if excitons preferentially localized to the lower energy state, the DBE emission would outcompete the STE emission at sufficiently high defect concentrations. While this competition between the STE and DBE emission mechanism has not been previously observed, existing reports of the coexistence of these mechanisms in $(NH_4)_2AgBr_3$ and Rb_2AgBr_3 have generally attributed the lower-energy emission mechanism to DBEs.[4]

The PLQYs measured for Gua_3CuCl_4, $Gua_7Cu_3Br_{10}$·3DMF, and $Gua_7Cu_3I_{10}$·3DMF were 17.21%, 12.50%, and 34.56%. Note that these PLQY values significantly underestimate the emission efficiencies because the broadband nature of emission in this family restricts the possible range of measurement; these

© 2022 The Authors. Advanced Photonics Research published by Wiley-VCH GmbH

26999293, 0, Downloaded from https://onlinelibrary.wiley.com/doi/10.1002/adpr.202200172, Wiley Online Library on [16/10/2022]. See the Terms and Conditions (https://onlinelibrary.wiley.com/terms-and-conditions) on Wiley Online Library for rules of use; OA articles are governed by the applicable Creative Commons License

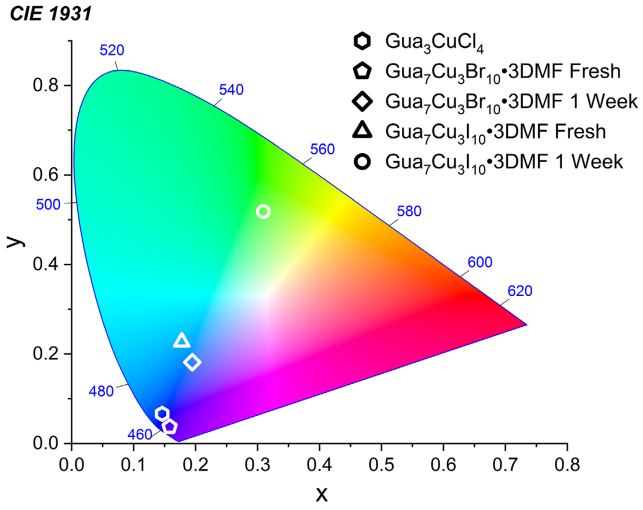

Figure 4. Commission Internationale de l'Eclairage (CIE) color coordinates of (red) Gua_3CuCl_4, (orange) fresh $Gua_7Cu_3Br_{10}$·3DMF, (yellow) $Gua_7Cu_3Br_{10}$·3DMF 1 week postsynthesis, (green) fresh $Gua_7Cu_3I_{10}$·3DMF, and (blue) $Gua_7Cu_3I_{10}$·3DMF 1 week postsynthesis.

PLQY measurements were cut off around 600 nm for $Gua_7Cu_3Br_{10}$·3DMF and $Gua_7Cu_3I_{10}$·3DMF because the PLE max for these samples are 303 and 314 nm, respectively. Interestingly, the high PLQY values for the solvates $Gua_7Cu_3Br_{10}$·3DMF and $Gua_7Cu_3I_{10}$·3DMF suggest that the incorporation of DMF into the crystal structures had no deleterious effect on quantum yield, for which quenching by solvent molecules can be a concern.[9] Although $Gua_7Cu_3I_{10}$·3DMF has by far the greatest PLQY, no significant trend is observed in the PLQY values across the three reported materials.

The excitation-dependent PL spectrum for $Gua_7Cu_3Br_{10}$·3DMF is shown in **Figure 5**a, which has an STE peak excitation wavelength maximum at 309 nm, consistent with the data in Figure 3b. However, the DBE emission peak is maximized under an excitation wavelength of 285 nm. Notably, as the excitation wavelength deviates from 309 nm, two behaviors are observed. As the excitation wavelength exceeds 309 nm, the STE and DBE peak intensities drop together. However, as the excitation wavelength drops below 309 nm, the DBE peak intensity increases while the STE peak falls. This deviation supports the assignment of the dual emission to two separate mechanisms, and the persistence of the low energy emission peak despite the reduction in STE emission peak intensity indicates that this low energy emission peak

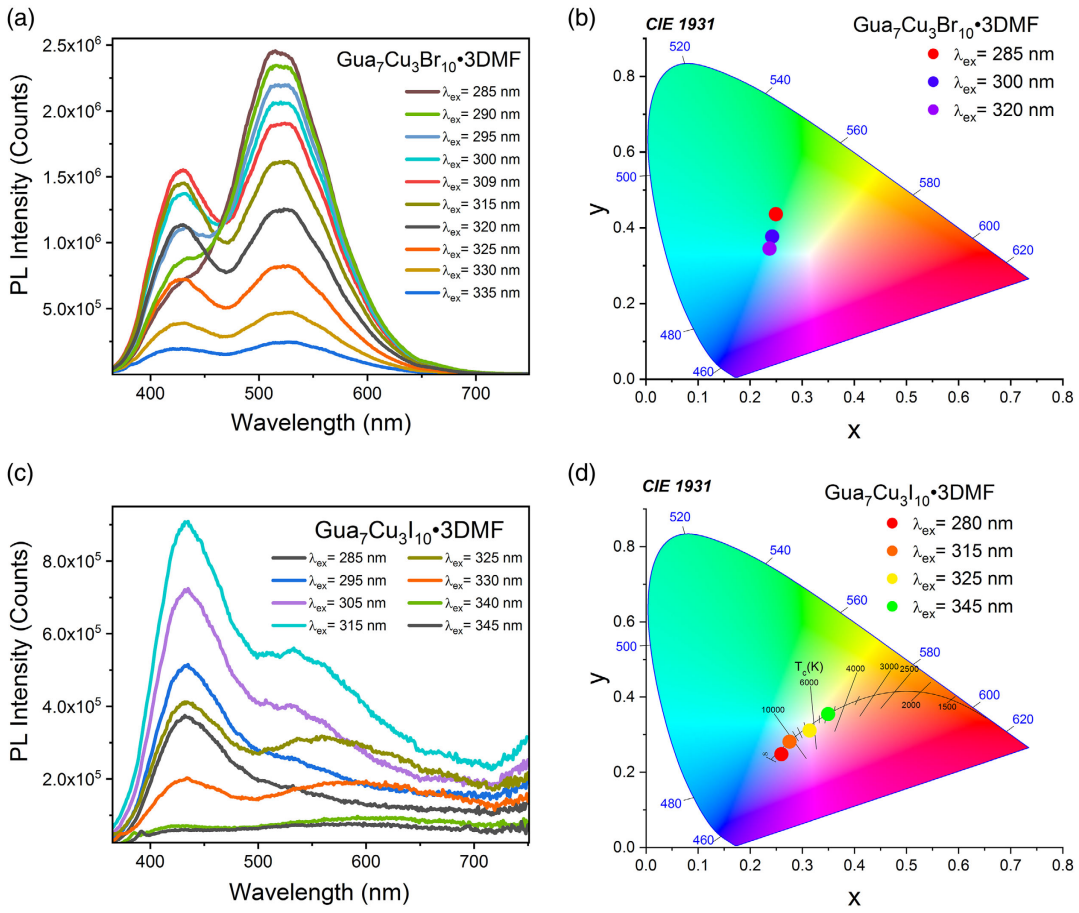

Figure 5. Excitation-dependent PL spectra for a) $Gua_7Cu_3Br_{10}$·3DMF and c) $Gua_7Cu_3I_{10}$·3DMF with CIE color coordinates for emission under selected excitation wavelengths shown for b) $Gua_7Cu_3Br_{10}$·3DMF and d) $Gua_7Cu_3I_{10}$·3DMF, respectively.

© 2022 The Authors. Advanced Photonics Research published by Wiley-VCH GmbH

26999293, 0, Downloaded from https://onlinelibrary.wiley.com/doi/10.1002/adpr.202200172, Wiley Online Library on [16/10/2022]. See the Terms and Conditions (https://onlinelibrary.wiley.com/terms-and-conditions) on Wiley Online Library for rules of use; OA articles are governed by the applicable Creative Commons License

Table 1. CIE color coordinates, D_{uv}, CCT, and CRI for $Gua_7Cu_3I_{10}$·3DMF emission at four different excitation wavelengths.

λ_{ex} [nm]	CIE *x*	CIE *y*	D_{uv}	CCT [K]	CRI
280	0.2597	0.2484	−0.0073	18 921	–
315	0.2753	0.2815	−0.0003	10 935	94
325	0.3140	0.3113	−0.0069	6579	–
345	0.3494	0.3551	−0.0001	4851	97

has an excitation response to a broad wavelength range. This broad response supports the assignment of the low energy peak to DBEs, which have been previously shown to respond to a broad range of excitation wavelengths.[14] CIE color coordinates for a selection of the excitation-dependent spectra for $Gua_7Cu_3Br_{10}$·3DMF are shown in Figure 5b, where we see a relatively minor color change between 285, 300, and 320 nm excitation wavelengths. Nevertheless, the transition from cyan to green emission indicates excitation-dependent PL tunability for $Gua_7Cu_3Br_{10}$·3DMF.

The excitation-dependent PL and corresponding CIE plots for $Gua_7Cu_3I_{10}$·3DMF are shown in Figure 5c,d, respectively. Here, we see a similar response to that observed for $Gua_7Cu_3Br_{10}$·3DMF. However, the CIE plot for $Gua_7Cu_3I_{10}$·3DMF shows more extreme sensitivity to excitation wavelength, with excitation wavelengths of 280, 315, 325, and 345 nm producing emission colors far apart on the CIE plot. Additionally, the CIE coordinates for $Gua_7Cu_3I_{10}$·3DMF match very closely to the Planckian white-light locus, with D_{uv} values of −0.0073, −0.0003, −0.0069, and −0.0001 for excitation wavelengths of 280, 315, 325, and 345 nm, respectively. These values fall within a range at which correlated color temperature (CCT) can be calculated, for which the CCT at excitation wavelengths of 280, 315, 325, and 345 nm is 18 921, 10 935, 6579, and 4851 K, respectively, indicating significant white-light tunability. Notably, the CCT of 4851 K at a 345 nm excitation wavelength falls within the CCT range of natural daylight (2500–6500 K).[15] Coupled with a D_{uv} value of −0.0001, this proximity to natural daylight results in a CRI of 97. The low D_{uv} of the spectrum under a 315 nm excitation wavelength also allows for calculation of a CRI value, which was 94 for the cool-white light of 10 935 K. The CIE coordinates as well as D_{uv}, CCT, and CRI values for these excitation wavelengths are shown in **Table 1**, and R1–R15 values for excitation wavelengths of 315 and 345 nm are presented in Table S5, Supporting Information.

In addition to the luminescence properties reported above, Gua_3CuCl_4 and $Gua_7Cu_3X_{10}$·3DMF also exhibit ASPL, a phenomenon observed in some other recently reported ternary copper(I) halides, including Rb_2CuX_3 and $AEP_2Cu_2X_6$·$2X{\cdot}2H_2O$.[2g,16] ASPL emission and ASPLE spectra are given in **Figure 6**, where Gua_3CuCl_4 exhibits an anti-Stokes emission maximum of 428 nm with an excitation wavelength maximum at 535 nm, yielding an anti-Stokes shift of 107 nm (0.5793 eV). $Gua_7Cu_3Br_{10}$·3DMF has an anti-Stokes emission maximum at a slightly shorter wavelength of 424 nm, with a correspondingly shorter excitation wavelength maximum at 514 nm and anti-Stokes shift of 90 nm (0.5121 eV). $Gua_7Cu_3I_{10}$·3DMF follows the same trend with an anti-Stokes emission maximum at 396 nm and corresponding excitation wavelength maximum at 499 nm but an anti-Stokes shift of 103 nm (0.6462 eV), closer to that of Gua_3CuCl_4. This trend indicates that the energy of anti-Stokes absorption and emission is affected by halide substitution, with larger halides tending to a higher anti-Stokes emission energy, but no significant trend is observed in the anti-Stokes shifts. Furthermore, a notable observation is made between the ASPL/ASPLE and PL/PLE spectra for $Gua_7Cu_3Br_{10}$·3DMF and $Gua_7Cu_3I_{10}$·3DMF (**Figure 7**). The emission maxima for the defect peaks of 497 and 517 nm for $Gua_7Cu_3Br_{10}$·3DMF and $Gua_7Cu_3I_{10}$·3DMF align closely with the anti-Stokes excitation wavelength maxima of 498 and 513 nm, respectively. The close alignment of the spectral features indicates a strong correlation between defect emission and anti-Stokes absorption.

To further probe the nature of the dual emission in $Gua_7Cu_3Br_{10}$·3DMF and $Gua_7Cu_3I_{10}$·3DMF, an experiment was performed to test whether the secondary emission peak resulted from the formation of halogen vacancies over time. A sample of $Gua_7Cu_3I_{10}$·3DMF was exposed to vacuum until the STE peak was completely replaced by 530 nm shoulder peak as shown in Figure 3d,e. Under vacuum, this tranformation was much accelerated and took place over only 2 days, rather than 1 week in a nitrogen-filled glove box. To test whether the change was the result of halogen vacancy formation, a selection of single crystals from the sample was exposed to an iodine-only atmosphere for approximately 15 min at room temperature. Under these conditions, a discoloration on the surface of the previously colorless crystals was observed as iodine adsorbed to the surface.

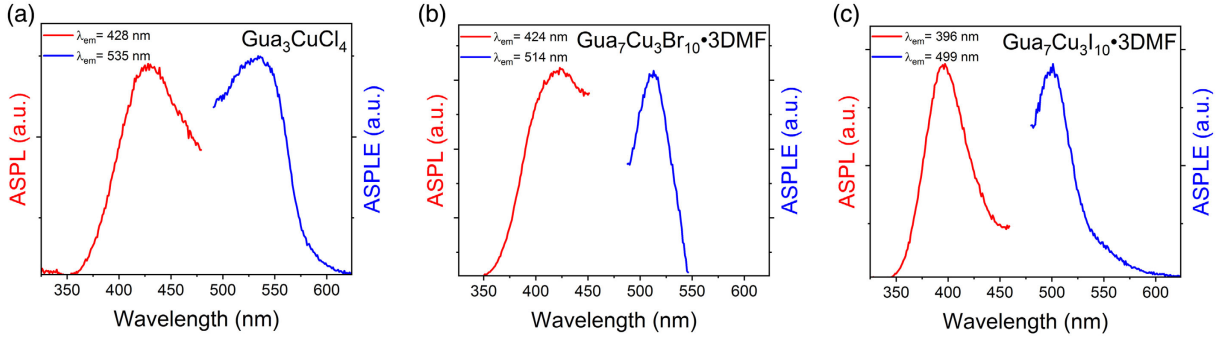

Figure 6. ASPL emission and ASPLE spectra for a) Gua_3CuCl_4, b) $Gua_7Cu_3Br_{10}$·3DMF, and c) $Gua_7Cu_3I_{10}$·3DMF.

© 2022 The Authors. Advanced Photonics Research published by Wiley-VCH GmbH

26999293, 0, Downloaded from https://onlinelibrary.wiley.com/doi/10.1002/adpr.202200172, Wiley Online Library on [16/10/2022]. See the Terms and Conditions (https://onlinelibrary.wiley.com/terms-and-conditions) on Wiley Online Library for rules of use; OA articles are governed by the applicable Creative Commons License

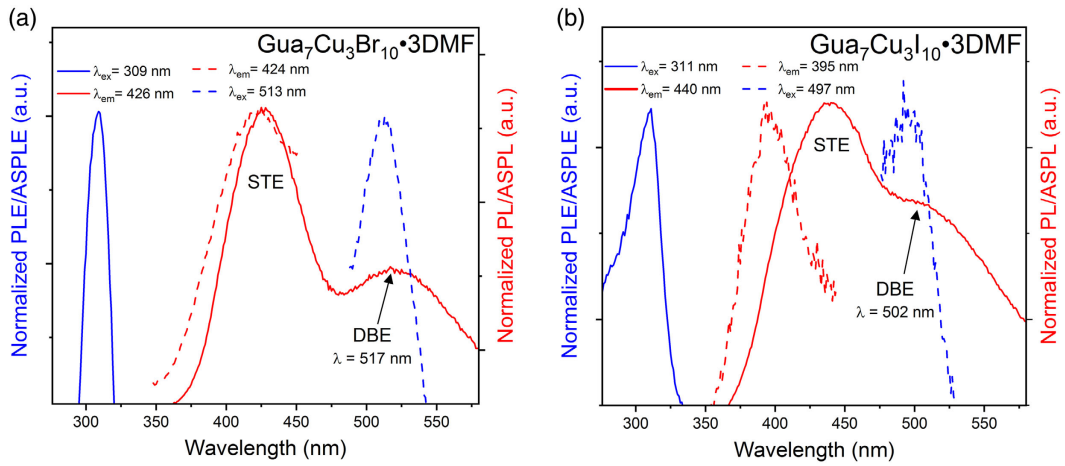

Figure 7. Normalized PL/PLE and ASPL/ASPLE for a) $Gua_7Cu_3Br_{10}$·3DMF and b) $Gua_7Cu_3I_{10}$·3DMF.

After 15 min, the crystals were extracted and quickly treated with isopropyl alcohol to remove the excess iodine, returning to nearly colorless. A PL spectrum was then taken on the iodine-treated crystals. The three PL spectra, including fresh $Gua_7Cu_3I_{10}$·3DMF, postvacuum $Gua_7Cu_3I_{10}$·3DMF, and iodine-treated $Gua_7Cu_3I_{10}$·3DMF, are superimposed in **Figure 8**. These experiments reveal that after 2 days in vacuum, the STE peak has been completely replaced by its 530 nm shoulder peak. However, after only 15 min iodine exposure, we see a return of the STE peak, this time as a shoulder of the 530 nm postvacuum peak. Although the change in PL after iodine exposure was relatively minor, any return of the STE peak suggests a reversion of the process by which the 530 nm peak came to dominate the PL spectrum. As this reversion took place under exposure to iodine at room temperature, this is strong evidence that the 530 nm postvacuum peak is caused by halogen vacancy formation, supporting our attribution of this peak to a halogen vacancy-localized DBE emission.

Time-resolved PL plots for $Gua_7Cu_3X_{10}$·3DMF are shown in Figure S10, Supporting Information, with relevant fitting parameters and specific lifetimes in Table S5, Supporting Information. $Gua_7Cu_3Br_{10}$·3DMF best fits a triexponential lifetime curve with

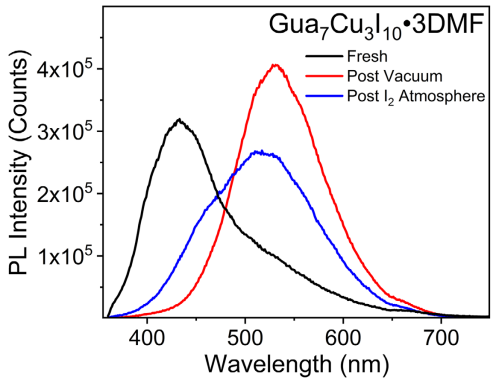

Figure 8. PL spectra of a single sample of $Gua_7Cu_3I_{10}$·3DMF (black) fresh, (red) postvacuum exposure, and (blue) postexposure to an iodine-only atmosphere.

lifetimes of 1.35 µs, 183 ns, and 58 ns, yielding an average lifetime of 1.20 µs, while $Gua_7Cu_3I_{10}$·3DMF best fits a biexponential lifetime curve with lifetimes of 161 and 28 ns, yielding a much shorter average lifetime of 147 ns. Notably, the $Gua_7Cu_3I_{10}$·3DMF sample used in this measurement was postvacuum, so it exhibited a single emission peak, which we attribute to DBEs. This lifetime is slightly shorter than the fastest previously reported defect-bound excitonic Ag(I) emitters, which have lifetimes ranging widely from 521 ns to 58.82 µs.[4] The longer average lifetime of $Gua_7Cu_3Br_{10}$·3DMF, which shows emission attributed to both STEs and DBEs, is consistent with previously reported STE Cu(I) emitters, which mostly have lifetimes ranging from 1 to 10 µs, with outliers as fast as 13.8 ns and as slow as 120 µs.[1c,1d,1g,1i,1k,2g,3a,5–8,17]

To measure the photostability of Gua_3CuCl_4 and $Gua_7Cu_3X_{10}$·3DMF, single-crystal samples were exposed to 450 W lamp light for 1 h, during which PLQY measurements were taken at 5 minute intervals. A comparison of the photostability for Gua_3CuCl_4, $Gua_7Cu_3Br_{10}$·3DMF, and $Gua_7Cu_3I_{10}$·3DMF is shown in Figure S11, Supporting Information. Here, a trend of decreasing photostability down the halide group is observed, with Gua_3CuCl_4 PL intensity falling the slowest and $Gua_7Cu_3I_{10}$·3DMF PL intensity falling the fastest. While Gua_3CuCl_4 has photostability comparable to that of high-efficiency blue-emitting Rb_2CuCl_3, for which PLQY drops by approximately 75% over 1 h,[2g] both $Gua_7Cu_3Br_{10}$·3DMF and $Gua_7Cu_3I_{10}$·3DMF exhibit PLQYs which drop by more than 85% over 1 h, indicating very poor photostability. Previously, however, substitution of the A^+ cation in ternary copper halides has resulted in dramatically improved photostability, with K_2CuCl_3 sporting a significantly increased photostability over Rb_2CuCl_3.[1d,2g] These previous stability improvements by A^+ cation substitution suggest that additional organic cations should be considered in place of $(CN_3H_6)^+$, which may lead to improvements in both air and photostability while maintaining the high PLQY and tunability seen in $Gua_7Cu_3X_{10}$·3DMF.

A comparison of various photophysical properties of the recently reported ternary copper(I) and silver halides is presented in **Table 2**. Here, notice that the K_2CuX_3 and Rb_2CuX_3 (X = Cl,

© 2022 The Authors. Advanced Photonics Research published by Wiley-VCH GmbH

26999293, 0, Downloaded from https://onlinelibrary.wiley.com/doi/10.1002/adpr.202200172, Wiley Online Library on [16/10/2022]. See the Terms and Conditions (https://onlinelibrary.wiley.com/terms-and-conditions) on Wiley Online Library for rules of use; OA articles are governed by the applicable Creative Commons License

Table 2. A comparison of the photophysical properties of selected all-inorganic and hybrid organic–inorganic ternary copper(I) and silver halides.[1d,1i,2g,3a,4,5c,6a,6c].

Compound	PL_{max} [nm]	PLE_{max} [nm]	Stokes shift [nm]	Lifetime [μs]	FWHM [nm]	Attribution	References
Gua_3CuCl_4	445	279	166	–	69	STE	This work
$Gua_7Cu_3Br_{10}$·3DMF[a)]	426 517	309	117 208	1.2	63 176	STE DBE	This work
$Gua_7Cu_3I_{10}$·3DMF[a)]	434 530	314	120 216	0.147	94 102	STE DBE	This work
$Gua_3Cu_2I_5$	481	254	227	1.98	125	STE	[6a]
$Gua_4Cu_4Br_8$	600	290	310	0.538	–	STE	[6c]
$MA_4Cu_2Br_6$	524	300	224	120	107	STE	[5c]
K_2CuCl_3	392	291	101	12.97	54	STE	[1d]
K_2CuBr_3	388	296	92	–	54	STE	[1d]
Rb_2CuCl_3	400	300	100	12.21	52	STE	[2g]
Rb_2CuBr_3	385	300	85	–	54	STE	[2g]
$CsCu_2Cl_3$	527	325	202	0.014	102	STE	[3a]
$CsCu_2Br_3$	533	325	208	0.018	106	STE	[3a]
$CsCu_2I_3$	576	325	251	0.062	126	STE	[3a]
$Cs_3Cu_2I_5$	445	290	155	0.464	–	STE	[1h]
$(NH_4)_2AgBr_3$	394 524	275	119 245	0.995	142	STE DBE	[4b]
$(NH_4)_2AgI_3$	534	303	231	1.25	114	DBE	[4b]
Rb_2AgCl_3	537	275	262	0.62	–	DBE	[4a]
Rb_2AgBr_3	363 485	283	202	0.77	–	STE DBE	[4a]
Rb_2AgI_3	485	304	181	1.15	–	DBE	[4a]
Cs_2AgCl_3	397	250	147	–	–	DBE	[4a]
Cs_2AgBr_3	524	292	232	58.82	–	DBE	[4a]
Cs_2AgI_3	595	310	285	14.67	–	DBE	[4a]

[a)]Exact photoluminescence parameters vary slightly with vacuum annealing time.

Br, I) families have PL emission maxima all around 400 nm. However, the copper halides with larger Cs^+, Gua^+, and MA^+ cations exhibit significantly redshifted PL maxima ranging from 445 nm for Gua_3CuCl_4 to 576 nm for $CsCu_2I_5$ despite the persistence of the excitation maxima around 300 nm. Because the emission maxima increase with the larger cations while the excitation maxima stay roughly the same, the same trend is seen in the Stokes shifts, where the Cs^+-, Gua^+-, and MA^+-based compounds have nearly double the Stokes shifts of the corresponding K^+ and Rb^+ copper(I) halides. A similar trend is seen in the breadth of PL peaks, with K_2CuX_3 and Rb_2CuX_3 (X = Cl, Br, I) having FWHM values at approximately half those of $CsCu_2X_3$ (X = Cl, Br, I), $MA_4Cu_2Br_6$, and the Gua^+ compounds. The same trends in A_2AgX_3 (A = NH_4, Rb, Cs; X = Cl, Br, I) are much more tenuous; however, with A^+ cation substitution having no consistent effect on PL. For example, in A_2AgI_3, NH_4^+ gives an emission maximum of 534 nm, Rb^+ gives a maximum of 485 nm, and Cs^+ gives a maximum of 595 nm, so no significant trend is seen. Nevertheless, a trend is observed in the copper(I) compounds, where PL emission maxima, Stokes shifts, and FWHMs are all consistently greater for the large, low-charge density cations of Gua^+, MA^+, and Cs^+ than for the smaller, more densely charged K^+ and Rb^+ cations. The stark differences in the PL properties of Cu(I) and Ag(I) halides are attributed to the defect-based PL emission of Ag(I) halides as compared to the Cu(I) halides, which predominantly exhibit STE-based emission. From this perspective, the preparation of $Gua_7Cu_3X_{10}$·3DMF acts as a bridge between the all-inorganic Cu(I) halides that demonstrate solely STE-based blue emission, and tunable light emitters based on Ag(I) halides that demonstrate multiexcitonic emission properties including emission due to the presence of halogen vacancies.

3. Conclusion

In this report, a simple method of preparation is presented for three new ternary copper(I) halides based on the guanidinium cation, which was chosen for its low charge density and disc-like shape to explore the effects of A^+ cation size and charge density on PL properties in copper(I) halides. In that exploration, we compared the results for our new Gua_3CuCl_4, $Gua_7Cu_3Br_{10}$·3DMF, and $Gua_7Cu_3I_{10}$·3DMF compounds with several other recently reported ternary copper halides and found that emission wavelength maxima, Stokes shifts, and FWHMs were all positively correlated with A^+ cation size. While excitation wavelength maxima remain around 300 nm (±50 nm), unlike the blue-emitting all-inorganic Cu(I) halides, the novel materials Gua_3CuCl_4, $Gua_7Cu_3Br_{10}$·3DMF, and $Gua_7Cu_3I_{10}$·3DMF reported here demonstrate very interesting PL properties, with

© 2022 The Authors. Advanced Photonics Research published by Wiley-VCH GmbH

26999293, 0, Downloaded from https://onlinelibrary.wiley.com/doi/10.1002/adpr.202200172, Wiley Online Library on [16/10/2022]. See the Terms and Conditions (https://onlinelibrary.wiley.com/terms-and-conditions) on Wiley Online Library for rules of use; OA articles are governed by the applicable Creative Commons License

the latter two sporting highly tunable dual emission attributed to both STEs and DBEs. We found that this dual emission was highly responsive to both excitation wavelength and vacuum annealing, during which the blue-emissive STE peak was slowly replaced by the yellow DBE peak. $Gua_7Cu_3I_{10}$·3DMF even showed a PLQY of up to 35.46% with CRI values up to 97 and correlated color temperature (CCT) values ranging from 4851 to 18 921 K depending on the excitation wavelength and vacuum treatment. We also report ASPL for these compounds, where we observe a strong correlation between anti-Stokes absorption and DBE emission, suggesting a possible defect-related mechanism for ASPL in this family of ternary Cu(I) halides. Although the stability of the novel materials reported here is low, with air, moisture, and photostability all being concerns, these materials offer insights into the nature of PL in copper(I) halides, and their desirable high-efficiency white-light emission properties are an indication that further exploration of organic cations in ternary copper(I) systems could beget promising alternatives to toxic lead halide perovskites and expensive rare-earth dopants for solid-state lighting applications.

4. Experimental Section

Materials and Methods: The starting reactants, guanidine hydrochloride (TCI, ≥98%), guanidine carbonate (99%, Aldrich), copper(I) chloride (≥99%, Sigma-Aldrich), copper(I) bromide (99%, Alfa Aesar), copper(I) iodide (≥99.5%, Sigma-Aldrich), hydrochloric acid (≥99.95%, 38 wt% in H_2O, EMD Millipore), hydrobromic acid (≥99.99%, 48 wt% in H_2O, Sigma-Aldrich), hydroiodic acid (99.95%, 57 wt% in H_2O, Sigma-Aldrich), and anhydrous *N,N*-dimethylformamide (DMF) (99.8%, Acros Organics), were all used as received. Synthesis of guanidine hydroiodide and guanidine hydrobromide was performed in open air, and all other manipulations of reactants and products were performed in a nitrogen-filled glove box.

Synthesis of Guanidinium Halides by Acid Titration: Guanidium halides (GuaX) (X = Br, I) were synthesized from guanidine carbonate via titration with hydrohalic acids. A 10% stoichiometric excess of the hydrohalic acid corresponding to the desired guanidinium halide was added dropwise to a round-bottom flask containing a slurry made with water (0.6 mL per 1 g guanidine carbonate). The resulting solution was left to sit for 30 min before being evaporated under vacuum using a rotary evaporator. The flask was then further dried under vacuum overnight before the resulting colorless powder was extracted and stored under nitrogen.

$Gua_7Cu_3X_{10}$·3DMF (X = Br, I) Single-Crystal Formation via Slow Cooling of a Saturated DMF Solution: $Gua_7Cu_3X_{10}$·3DMF single crystals were prepared by mixing stoichiometric amounts of GuaX and CuX in DMF. The reagents (combined 2.5 g) were added to a 20 mL glass scintillation vial containing a stir bar and mixed with DMF (1 mL, X = Br or 0.75 mL, X = I). The vial was then capped and heated at 85–100 °C with stirring until all reagents were fully dissolved. The stir bar was then removed, and the vials were recapped before being cooled to 75 °C over 1 h. The solution was slowly cooled to room temperature over 24 h, yielding colorless block crystals of $Gua_7Cu_3X_{10}$·3DMF of up to 1 cm in length. These block crystals were extracted from the DMF solution before being dried thoroughly with filter paper.

Gua_3CuCl_4 Single-Crystal Formation via Slow Cooling of a Saturated Hydrochloric Acid Solution: Gua_3CuCl_4 single crystals were prepared by a variation of the above slow cooling in DMF; however, a hydrochloric acid solution was used instead. Stoichiometric amounts of GuaCl and CuCl were added to a 20 mL glass scintillation vial in a nitrogen-filled glove box and mixed with hydrochloric acid (1 mL, 38 wt%) by addition through a rubber septum. The vial was then removed from the glove box before nitrogen flow through the vial was established by piercing the septum with nitrogen inflow and outflow cannulas. The mixture was heated to 90 °C, and a minimal amount of hydrochloric acid was added to fully dissolve the reactants. The solution was then slowly cooled to room temperature over 24 h, yielding colorless block crystals of Gua_3CuCl_4. These crystals were extracted from the acid solution in a nitrogen-filled glove box before being dried thoroughly with filter paper.

Treatment of $Gua_7Cu_3I_{10}$·3DMF Single Crystals with Iodine: Single crystals of $Gua_7Cu_3I_{10}$·3DMF were transferred under nitrogen into a sealed piece of Schlenk glassware containing two connected tubes. The apparatus was then transferred to a Schlenk line, after which nitrogen flow through the apparatus was established. Solid elemental iodine (≈1 g) was added to the second tube, and vacuum was pulled on the apparatus before sealing to induce an iodine-only atmosphere. The single crystals of $Gua_7Cu_3I_{10}$·3DMF were exposed to iodine for 15 min before being removed and briefly washed with isopropyl alcohol under nitrogen. PL measurements were taken on the same sample of $Gua_7Cu_3I_{10}$·3DMF single crystals before and after iodine exposure and compared.

PXRD Measurements: PXRD measurements were taken on a Rigaku Miniflex600 Diffractometer equipped with D/tex detector and a Ni-filtered Cu Kα radiation source. All data were collected at room-temperature, and angle ranges used were 3°–90° (2θ) with a step size of 0.02° and a speed of 20° min^{-1}. The obtained patterns were refined using the decomposition method in PDXL-2 software. For air stability measurements, powdered samples of Gua_3CuCl_4 and $Gua_7Cu_3X_{10}$·3DMF were left in a laboratory drawer under ambient conditions (relative humidity of 30%) for 24 h, during which periodic PXRD measurements were taken.

SCXRD Measurements: SCXRD measurements were performed using a D8 Quest κ-geometry diffractometer with a Bruker Photon II cmos area detector and an Incoatec I μs microfocus Mo Kα source ($\lambda = 0.71073$ Å). The samples were cooled to 100 K for data collection, and the structures were solved by dual-space methods and refined by full-matrix least-squares methods on F^2. The positions of hydrogens bonded to carbons and nitrogens were initially determined by geometry and were refined using a riding model. Nonhydrogen atoms were refined with anisotropic displacement parameters while hydrogen atom displacement parameters were set to 1.2 (1.5 for methyl) times the isotropic equivalent distance parameters of the bonded atoms. Details of the data collection and crystallographic parameters are given in Table S1, Supporting Information. Atomic coordinates, equivalent isotropic displacement parameters, and selected interatomic distances and bond angles are provided in Table S2–S4, Supporting Information. Additional information on the crystal structures can be obtained in the form of crystallographic information files (CIF), which were deposited in the Cambridge Crystallographic Data Centre (CCDC) database with deposition numbers 2169657 and 2169658 and provided as Supporting Information.

TGA/DSC Measurements: Simultaneous TGA and DSC measurements were performed on 5–10 mg of powdered $Gua_7Cu_3X_{10}$·3DMF (X = Br, I) using a TA instruments SDT 650 thermal analyzer system. Samples were placed in a 90 μL alumina crucible, capped, and heated from 25 to 650 °C (5 °C min^{-1}) under nitrogen gas (100 mL min^{-1}).

Optical Measurements: Room-temperature PL and PLE measurements were performed on single crystals of Gua_3CuCl_4 and $Gua_7Cu_3X_{10}$·3DMF using a Jobin Yvon Fluorolog-3 spectrofluorometer (HORIBA) with a Xenon lamp (280–750 nm). CIE color coordinates and plots were generated from PL spectra using the Origin 2019 software. For TRPL, a time-correlated single photon counting system with a DeltaHub DH-HT high throughput TCSPC controller and NanoLED NL-C2 pulsed diode controller was used. The TRPL light source was a NanoLED diode with a <1.2 ns pulse duration. Fitting parameters are shown in Table S1, Supporting Information, and the fitting equations used were

$$I(t) = \sum_{i=1}^{n} A_i \exp\left(\frac{-t}{\tau_i}\right) \quad (1)$$

$$\tau_{avg} = \left(\sum_{i=1}^{n} A_i \tau_i^2\right)\left(\sum_{i=1}^{n} A_i \tau_i\right)^{-1} \quad (2)$$

© 2022 The Authors. Advanced Photonics Research published by Wiley-VCH GmbH

26999293, 0, Downloaded from https://onlinelibrary.wiley.com/doi/10.1002/adpr.202200172, Wiley Online Library on [16/10/2022]. See the Terms and Conditions (https://onlinelibrary.wiley.com/terms-and-conditions) on Wiley Online Library for rules of use; OA articles are governed by the applicable Creative Commons License

Supporting Information

Supporting Information is available from the Wiley Online Library or from the author.

Acknowledgements

This work was supported by the University of Oklahoma (OU) startup funds and by funds provided by the National Science Foundation (DMR-2045490). Financial support was provided by the University of Oklahoma Libraries' Open Access Fund. The structure of Gua_3CuCl_4 was determined by T.D.C., and the structure of $Gua_7Cu_2Br_{10}{\cdot}3DMF$ was determined by Dr. Douglas R. Powell. The diffractometer used for SCXRD measurements was purchased through funds from the National Science Foundation (CHE-1726630). The authors would also like to thank Hadiah Fattal for performing TGA/DSC measurements and Nancy Wang for her assistance in material preparation.

Conflict of Interest

The authors declare no conflict of interest.

Author Contributions

This manuscript was written through the contributions of each author. All authors have approved the final version of this manuscript. I.W.G. prepared the samples and performed PXRD measurements; I.W.G., T.D.C., and T.M.M. performed and analyzed the optical measurements; and B.S. conceived and supervised the work.

Data Availability Statement

The data that support the findings of this study are available from the corresponding author upon reasonable request.

Keywords

anti-Stokes, copper halides, lead-free halides, light emission, photoluminescence

Received: June 27, 2022
Revised: July 7, 2022
Published online:

[1] a) S. Lu, Q. Zhou, Y. Ouyang, Y. Guo, Q. Li, J. Wang, *Nat. Commun.* **2018**, *9*, 3405; b) Z. Zhang, R. Zhao, S. Teng, K. Huang, L. Zhang, D. Wang, W. Yang, R. Xie, N. Pradhan, *Small* **2020**, *16*, 2004272; c) X. Mo, T. Li, F. Huang, Z. Li, Y. Zhou, T. Lin, Y. Ouyang, X. Tao, C. Pan, *Nano Energy* **2020**, *81*, 105570; d) T. D. Creason, T. M. McWhorter, Z. Bell, M.-H. Du, B. Saparov, *Chem. Mater.* **2020**, *32*, 6197; e) G. Seo, H. Jung, T. D. Creason, V. Yeddu, M. Bamidele, E. Echeverria, J. Lee, D. McIlroy, B. Saparov, D. Y. Kim, *ACS Energy Lett.* **2021**, *6*, 2584; f) J. Luo, M. Hu, G. Niu, J. Tang, *ACS Appl. Mater. Interfaces* **2019**, *11*, 31575; g) B. Yang, L. Yin, G. Niu, J. H. Yuan, K. H. Xue, Z. Tan, X. S. Miao, M. Niu, X. Du, H. Song, E. Lifshitz, J. Tang, *Adv. Mater.* **2019**, *31*, 1904711; h) T. Jun, K. Sim, S. Iimura, M. Sasase, H. Kamioka, J. Kim, H. Hosono, *Adv. Mater.* **2018**, *30*, 1804547; i) T. Jun, K. Sim, S. Iimura, M. Sasase, H. Kamioka, J. Kim, H. Hosono, *Adv. Mater.* **2018**, *30*, 1804547; j) J. Sun, J. Yang, J. I. Lee, J. H. Cho, M. S. Kang, *J. Phys. Chem. Lett.* **2018**, *9*, 1573; k) W. Gao, L. Yin, J.-H. Yuan, K.-H. Xue, G. Niu, B. Yang, Q. Hu, X. Liu, J. Tang, *Org. Electron.* **2020**, *86*, 105903; l) S. Chakraborty, W. Xie, N. Mathews, M. Sherburne, R. Ahuja, M. Asta, S. G. Mhaisalkar, *ACS Energy Lett.* **2017**, *2*, 837; m) M. Sharma, A. Yangui, V. R. Whiteside, I. R. Sellers, D. Han, S. Chen, M. H. Du, B. Saparov, *Inorg. Chem.* **2019**, *58*, 4446.

[2] a) M. A. Green, A. Ho-Baillie, H. J. Snaith, *Nat. Photonics* **2014**, *8*, 506; b) Y. Wei, Z. Cheng, J. Lin, *Chem. Soc. Rev.* **2019**, *48*, 310; c) M. Cai, Y. Wu, H. Chen, X. Yang, Y. Qiang, L. Han, *Adv. Sci.* **2017**, *4*, 1600269; d) C. H. A. Li, Z. Zhou, P. Vashishtha, J. E. Halpert, *Chem. Mater.* **2019**, *31*, 6003; e) Y. Li, K. Yang, *Energy Environ. Sci.* **2019**, *12*, 2233; f) L. K. Ono, Y. Qi, S. Liu, *Joule* **2018**, *2*, 1961; g) T. D. Creason, A. Yangui, R. Roccanova, A. Strom, M.-H. Du, B. Saparov, *Adv. Opt. Mater.* **2020**, *8*, 1901338; h) T. C. Sum, N. Mathews, *Energy Environ. Sci.* **2014**, *7*, 2518; i) R. Roccanova, M. Houck, A. Yangui, D. Han, H. Shi, Y. Wu, D. T. Glatzhofer, D. R. Powell, S. Chen, H. Fourati, A. Lusson, K. Boukheddaden, M.-H. Du, B. Saparov, *ACS Omega* **2018**, *3*, 18791; j) M. Wu, N. Haji Ladi, Z. Yi, H. Li, Y. Shen, M. Wang, *Energy Technol.* **2019**, *8*, 1900744.

[3] a) R. Roccanova, A. Yangui, G. Seo, T. D. Creason, Y. Wu, D. Y. Kim, M.-H. Du, B. Saparov, *ACS Mater. Lett.* **2019**, *1*, 459; b) L. Protesescu, S. Yakunin, M. I. Bodnarchuk, F. Krieg, R. Caputo, C. H. Hendon, R. X. Yang, A. Walsh, M. V. Kovalenko, *Nano Lett.* **2015**, *15*, 3692.

[4] a) P. Kumar, T. D. Creason, H. Fattal, M. Sharma, M.-H. Du, B. Saparov, *Adv. Funct. Mater.* **2021**, *31*, 2104941; b) T. D. Creason, H. Fattal, I. W. Gilley, T. M. McWhorter, M.-H. Du, B. Saparov, *ACS Mater. Au* **2021**, *1*, 62.

[5] a) X. Zhao, G. Niu, J. Zhu, B. Yang, J. H. Yuan, S. Li, W. Gao, Q. Hu, L. Yin, K. H. Xue, E. Lifshitz, X. Miao, J. Tang, *J. Phys. Chem. Lett.* **2020**, *11*, 1873; b) S. Fang, H. Li, Y. Xie, H. Li, Y. Wang, Y. Shi, *Small* **2021**, *17*, 2103831; c) H. Peng, S. Yao, Y. Guo, R. Zhi, X. Wang, F. Ge, Y. Tian, J. Wang, B. Zou, *J. Phys. Chem. Lett.* **2020**, *11*, 4703.

[6] a) H. Peng, X. Wang, Y. Tian, B. Zou, F. Yang, T. Huang, C. Peng, S. Yao, Z. Yu, Q. Yao, G. Rao, J. Wang, *ACS Appl. Mater. Interfaces* **2021**, *13*, 13443; b) Z. Song, B. Yu, G. Liu, L. Meng, Y. Dang, *J. Phys. Chem. Lett.* **2022**, *13*, 2567; c) Z. Song, B. Yu, L. Meng, G. Liu, Y. Dang, *Mater. Adv.* **2022**, *3*, 2447; d) S. Wu, Z. Li, J. Zhang, T. Liu, Z. Zhu, A. K. Jen, *Chem. Commun.* **2019**, *55*, 4315; e) Y. Xu, J. Hu, X. Xiao, H. He, G. Tong, J. Chen, Y. He, *Inorg. Chem. Front.* **2022**, *9*, 494.

[7] L. Lian, M. Zheng, P. Zhang, Z. Zheng, K. Du, W. Lei, J. Gao, G. Niu, D. Zhang, T. Zhai, S. Jin, J. Tang, X. Zhang, J. Zhang, *Chem. Mater.* **2020**, *32*, 3462.

[8] E. N. Kovalenko, O. N. Yunakova, N. N. Yunakov, *Low Temp. Phys.* **2021**, *47*, 427.

[9] S. Boothroyd, A. Kerridge, A. Broo, D. Buttar, J. Anwar, *Cryst. Growth Des.* **2018**, *18*, 1903.

[10] R. Teraoka, Y. Matsuda, I. Sugimoto, *Iryo Yakugaku (Jpn. J. Pharm. Health Care Sci.)* **2002**, *28*, 521.

[11] M.-H. Du, *ACS Energy Lett.* **2020**, *5*, 464.

[12] P. Makuła, M. Pacia, W. Macyk, *J. Phys. Chem. Lett.* **2018**, *9*, 6814.

[13] a) D. Balbakov, V. F. Pichugin, *Tomsk. Politekh. Inst.* **1983**; b) Y. Liu, K. Palotas, X. Yuan, T. Hou, H. Lin, Y. Li, S. T. Lee, *ACS Nano* **2017**, *11*, 2060.

© 2022 The Authors. Advanced Photonics Research published by Wiley-VCH GmbH

26999293, 0, Downloaded from https://onlinelibrary.wiley.com/doi/10.1002/adpr.202200172, Wiley Online Library on [16/10/2022]. See the Terms and Conditions (https://onlinelibrary.wiley.com/terms-and-conditions) on Wiley Online Library for rules of use; OA articles are governed by the applicable Creative Commons License

[14] A. O. Murzin, N. I. Selivanov, V. O. Kozlov, I. I. Ryzhov, T. Miyasaka, A. V. Emeline, Y. V. Kapitonov, *Adv. Opt. Mater.* **2021**, *9*, 2001327.
[15] Y. H. Kim, P. Arunkumar, S. H. Park, H. S. Yoon, W. B. Im, *Mater. Sci. Eng., B* **2015**, *193*, 4.
[16] J. H. Wei, Y. W. Yu, J. B. Luo, Z. Z. Zhang, D. B. Kuang, *Adv. Opt. Mater.* **2022**, 2200724.
[17] a) W. Gao, G. Niu, L. Yin, B. Yang, J.-H. Yuan, D. Zhang, K.-H. Xue, X. Miao, Q. Hu, X. Du, J. Tang, *ACS Appl. Electron. Mater.* **2020**, *2*, 2242; b) R. Roccanova, A. Yangui, H. Nhalil, H. Shi, M.-H. Du, B. Saparov, *ACS Appl. Electron. Mater.* **2019**, *1*, 269; c) F. Zhang, W. Liang, L. Wang, Z. Ma, X. Ji, M. Wang, Y. Wang, X. Chen, D. Wu, X. Li, Y. Zhang, C. Shan, Z. Shi, *Adv. Funct. Mater.* **2021**, *31*, 2105771.

© 2022 The Authors. Advanced Photonics Research published by Wiley-VCH GmbH

26999293, 0, Downloaded from https://onlinelibrary.wiley.com/doi/10.1002/adpr.202200172, Wiley Online Library on [16/10/2022]. See the Terms and Conditions (https://onlinelibrary.wiley.com/terms-and-conditions) on Wiley Online Library for rules of use; OA articles are governed by the applicable Creative Commons License